Article

Secondary Motion of Non-Spherical Particles in Gas Solid Flows

Cihan Ates *, Joel Arweiler, Habeb Hadad, Rainer Koch and Hans-Jörg Bauer

Institute of Thermal Turbomachinery, Karlsruhe Institute of Technology (KIT), 76137 Karlsruhe, Germany
* Correspondence: cihan.ates@kit.edu; Tel.: +49-72160844703

Abstract: Objective of this study is to investigate the effect of secondary motion of particles in multiphase gas-solid flows parametrically and test the relative impacts of particle shape and orientation information on particle distribution. For that purpose, predictive accuracies of simplified drag coefficient models are assessed for the conditions relevant to a wood recovery plant operating at dilute flow regime. After demonstrating the strong impact of the shape and orientation information on the force balance for single particles, we compared the steady state Eulerian-Lagrangian simulation results for particle volume fractions, residence times and particle diameter distributions within the chamber for different (i) superficial gas velocities (5 m/s, 7.5 m/s), (ii) orientation tendencies and (iii) particle shapes. Transient simulations are performed until the system reaches steady state conditions by monitoring the mass flow rates of the particulate phases leaving the chamber. The secondary motion of non-spherical particles is represented by stochastic sampling from the available experimental data. Analysis of the force balance on single particles revealed log-scale variations if the orientation of the particles with respect to flow fluctuates. Variations in the single particle force balances are found to be still visible in the CFD analysis, where the secondary motion of particles drastically changed the particle distribution in the chamber. The native non-spherical model which only accounts for the shape correction was found to over-predict the entrainment, leading to a significantly different particle volume fraction and diameter distributions. Spherical particle assumption also caused significant errors in the particle distribution, which increases as aspect ratio of the cylindrical particle diverges from one. Results show that particle orientation statistics are extremely important to capture the particle mixing and segregation patterns at dilute regime, which cannot be captured with such simplifying assumptions.

Keywords: non-spherical particle; particle orientation; secondary motion; drag coefficient; particle segregation; Hölzer-Sommerfeld correlation

1. Introduction

Particles in a gas-solid flow are usually non-spherical, having irregular shapes and exhibit poly-dispersed size distributions. This simple fact snowballs into highly nonlinear behaviour in practice as the geometry of the particle affects the characteristics of the boundary layer, as well as the generation and dissipation of wake vortices. In turbulent flow regimes, which corresponds to a significant share of the industrial gas-solid flows, relative motion between the particles become large and the particulate phase can be regarded as a dilute suspension, analogous to the rarefied gas flow. Herein, the force balance is typically dominated by the pressure distribution and the viscous stresses on the particle surface, known as the drag force dating back to the Newton's experiments in 1710. Since then, a colossal amount of experimental data on the drag coefficient for spherical particles has been compiled and molded into equations such as Ergun [1], Wen-Yu [2], Syamlal–O'Brien [3] and Huilin-Gidaspow [4] models. The model equation library has been further expanded via direct numerical simulations (DNS) including Hill et al. [5], Beetstra et al. [6], Tenneti et al. [7] and Tang et al. [8]. A detailed comparative analysis of these drag models

can be found in [9]. It is seen that the majority of the literature still relies on the empirical correlations developed for spherical particles for capturing the gas-solid phase interactions in Eulerian-Eulerian or Eulerian-Lagrangian frameworks [10], where the particulate phase is usually represented by single representative diameter, despite the fact that particles are poly-disperse and have irregular shapes in practice.

In the last three decades, however, there has been a growing interest in the characterization of fluid-particle interactions for non-spherical particles [11]. Herein, theoretical studies (CFD-based approximations, Lattice Boltzmann methods, DNS) typically focus on drag formulations at low Re number flows for a specific particle shape [12–19]. On the other hand, empirical studies usually cover a much wider Re number range and can be generalized to multiple particle shapes. Popular formulations include the models of Haider-Levenspiel [20], Ganser [21], Tran-Cong [22], Dioguardi-Mele [23] and Bagheri-Bonadonna [24], some of which are offered as non-spherical particle models in the commercial software toolbox, hence commonly deployed in Eulerian-Eulerian or Eulerian-Lagrangian simulations of large scale systems. These models, however, ignore the particle orientation with respect to the flow direction (i.e., nutation angle) and only account for the shape information in the form of sphericity. Such an approach works well for spherical particles, as there is no preferred direction with respect to their trajectories (i.e., they have no preferred orientation). Non-spherical particles, however, experience shape induced lift and orientation dependent lift and drag forces. In particular, the drag experienced by the particles can differ drastically with the changing projected area, which is inherently is strong function of both the shape and orientation. As a result, non-spherical particles exhibit secondary motions including periodic oscillations, gliding and tumbling superimposed on the steady movement of the particles. It is initiated by the onset of wake instability and triggered for particle Reynolds (Re_p) number > 100 [10]. Although the secondary motion can lead to complex trajecotry and orientation patterns for single particles in an observed time frame, it has been shown that particles also in exhibit statistically preferred direction depending on the particle Reynolds (Re_p) number [10,25], thus can be taken advantage of to formulate an orientation dependent drag force formulation.

In their pioneering work, Hölzer and Sommerfeld [26] introduced a general drag model that takes both the particle orientation and shape (sphericity) into account. They showed that the addition of the orientation information in their model reduces the mean relative deviation from 383% (Haider-Levenspiel) and 343% (Ganser) to 14% compared to experimental measurements for a range of particle shapes. In particular, the proposed model can capture the fluid-particle interactions even for disk-like particles (16% error). The error increases up to 2000% and 1800% in the case of the previous models that only consider the shape information (i.e., sphericity). The striking importance of particle orientation has been further explored in the following experimental [27] and DNS studies [28], the outcomes of which show significant variations in the measured/computed drag coefficients with changing orientation for practically relevant conditions (at high particle Re numbers). Similar outcomes were found in DEM-gas flow simulations in pneumatic conveying [29], fluidization of cylindrical disk-like [30] and elongated particles [31]. A similar observation has also been made in a recent work [32], in which the previous drag coefficient models were reported to fail to predict the measured drag coefficients for non-spherical reference particles. For more comprehensive review of the motion of particles in gas-solid flows, the reader is referred to [33–38] for turbulent-particulate interactions, refs. [14,23,24,39,40] for modelling with non-spherical particles, [10,41] for secondary motion of particles and [39,42,43] for a more general overview.

Our cumulative understanding of the gas-particle flows points out that macroscopic behaviour of such systems further depends on the shape and particle orientation especially at high Re, which is typically ignored in practice to make particle representation simple. In an attempt to highlight the dilemma and propose a time and cost effective remedy within the Eulerian-Lagrangian simulation framework, we investigated the effect of secondary motion of particles in multi-phase gas-solid flows parametrically. The dilute flow regime for

a wood recycling problem is selected as a case study to identify the influence of the orientation information on the particle-flow interactions. This is done by deploying probability density functions for particle orientation sampling within the user-defined drag model based on Hölzer-Sommerfeld correlation [26] in ANSYS environment. We demonstrate the large impact of particle shape and orientation for alternative scenarios and assessed the predictive accuracy of simplifying assumptions commonly used in the community.

2. Materials and Methods

2.1. Force Balance Calculations

The case study of interest is the particle separation under dilute flow conditions, for which the particle segregation and the entrainment strongly depend on the balance between the drag, gravitational and the buoyancy forces for mm-cm range particles. One goal of the study is to assess how much the predictions from simple force ratio computations correlate with the predictions of the detailed CFD simulations with respect to the secondary motion tendencies of particles. For that purpose, we computed the force balance acting on individual particle for a range of particle and flow properties:

$$R = \frac{3C_D \rho_f u^2}{4(\rho_p - \rho_f)g d_{eq}} \tag{1}$$

in which the drag coefficient is calculated via the Hölzer-Sommerfeld correlation [26]:

$$C_D = \frac{8}{Re_p} \frac{1}{\sqrt{\phi_\perp}} + \frac{16}{Re_p} \frac{1}{\sqrt{\phi}} + \frac{3}{\sqrt{Re_p}} \frac{1}{\phi^{3/4}} + 0.42 \times 10^{0.4(-log\phi)^{0.2}} \frac{1}{\phi_\perp} \tag{2}$$

$$Re_p = \frac{u d_{eq}}{\nu_f} \tag{3}$$

Herein, $\phi_\perp$ is the crosswise sphericity, which defines the ratio between the constant cross-sectional area of the volume equivalent sphere and the projected cross-sectional area of the considered particle perpendicular to the flow direction. For cylindrical particles, the $\phi_\perp$ and the ϕ can be readily calculated for a sampled nutation angle θ, aspect ratio (AR) at a given equivalent diameter d_{eq}. Hence, the force ratio R becomes a function of:

$$R = f(\rho_p, u, d_{eq}, AR, \theta) \tag{4}$$

It should be noted that the drag correlation is the simplified version of the proposed equation in the original study [26] which only includes $\phi_\perp$ in addition to sphericity ϕ. In other words, the lengthwise sphericity $\phi_{||}$ in the first term $(8/Re_p 1/\sqrt{\phi_{||}})$ is replaced by the crosswise sphericity as discussed by the authors in the same study [26].

2.2. Modelling of Multiphase Flow

All simulations (2D) are done with ANSYS Fluent, where the gas phase is treated as a Eulerian continuum and the solid phase is represented by discrete Lagrangian parcels. Such a coupling scheme is referred as CFD-DPM (Discrete particle Method) in literature, which can be interpreted as a simplified CFD-DEM model simplifying the particle-particle interactions by considering the particle bundles as point particles. Therefore, this simplifying assumption is only valid when the particle volume fractions are low as in pneumatic conveying, in which particle-particle collision does not have a significant role. Trajectories of particle bundles (i.e., parcels) are computed individually at specified intervals during the fluid phase calculation in the Lagrangian frame of reference:

$$m_p \frac{d\vec{u}_p}{dt} = m_p \frac{\vec{u} - \vec{u}_p}{\tau_r} + m_p \frac{\vec{g}(\rho_p - \rho)}{\rho_p} + \vec{F} \tag{5}$$

where m_p is the particle mass, u_p is the particle velocity, first term on the right-hand side of the equation is the drag force and $\vec{F}$ denotes all other forces affecting the trajectory of the particle. It should be noted that τ_r is the particle relaxation time and calculated from:

$$\tau_r = \frac{\rho_p d_p^2}{18\mu} \frac{24}{C_d Re_p} \tag{6}$$

where d_p is the equivalent article diameter and Re_p is the relative particle Re number:

$$Re_p = \frac{\rho d_p |\vec{u} - \vec{u}_p|}{\mu} \tag{7}$$

It should be noted that during the trajectory calculations, instantaneous value of the fluctuating gas flow velocity $\vec{u}$ is used rather than the mean fluid phase velocity (i.e., stochastic tracking).

In Fluent, prediction of turbulent dispersion of particles is done by integrating the trajectory equations along the particle path. Integral time scale is predicted according to the selected turbulence model, which was selected as Realizable $k - \epsilon$ considering the grid size limitations near the wall. The other simple forces that can be included within DPM module are the virtual mass force and the pressure gradient forces, which has neglected in the current implementation due the difference in densities ($\rho/\rho_p \ll 1$). We also ignored the forces due to moving reference frames, thermophoretic, Brownian, Saffman and Magnus forces, considering the studied particle size range in the nonreactive case study at room temperature.

For the drag forces, two Fluent native drag laws are used together with the custom drag coefficient model, i.e., the Hölzer-Sommerfeld correlation. The spherical drag model has the form:

$$C_d = a_1 + \frac{a_2}{Re_p} + \frac{a_3}{Re_p^2} \tag{8}$$

where the model parameters are taken from Morsi and Alexander [44]. The non-spherical model is based on the study of Haider and Levenspiel [20]:

$$C_d = \frac{24}{Re_p}(1 + b_1 Re_p^{b_2}) + \frac{b_3 Re_p}{b_4 + Re_p} \tag{9}$$

Coupling of the phases is done via mixture model approach, where the conservation equations for mass and momentum is solved for the mixture:

$$\frac{\partial}{\partial t}(\rho_m) + \nabla \cdot (\rho_m \vec{v}_m) = 0 \tag{10}$$

$$\frac{\partial}{\partial t}(\rho_m \vec{v}_m) + \nabla \cdot (\rho_m \vec{v}_m \vec{v}_m) = -\nabla p + \nabla \cdot \left[\mu_m\left(\nabla \vec{v}_m + \nabla \vec{v}_m^T\right)\right] + \rho_m \vec{g} + \vec{F} - \nabla \cdot \left(\sum_{k=1}^{n} \alpha_k \rho_k \vec{v}_{dr,k} \vec{v}_{dr,k}\right) \tag{11}$$

where subscript m denotes the mixture. $\vec{v}_m$ and ρ_m are the mass averaged velocity and mixture density, respectively:

$$\vec{v}_m = \frac{\sum_{k=1}^{n} \alpha_k \rho_k \vec{v}_k}{\rho_m} \tag{12}$$

$$\rho_m = \sum_{k=1}^{n} \alpha_k \rho_k \tag{13}$$

The term $\vec{v}_{dr,k}$ in the momentum equation is the drift velocity for the particulate phase $k(\vec{v}_{dr,k} = \vec{v}_k - \vec{v}_m)$. The volume fraction equations are solved for the secondary particulate phases from the continuity equation:

$$\frac{\partial}{\partial t}\left(\alpha_p \rho_p\right) + \nabla \cdot \left(\alpha_p \rho_p \vec{v}_m\right) = -\nabla \cdot \left(\alpha_p \rho_p \vec{v}_{dr,p}\right) + \sum_{q=1}^{n}\left(\dot{m}_{qp} - \dot{m}_{pq}\right) \tag{14}$$

where p denotes the particulate phase. In the current study, Gidaspow is used for calculating the granular viscosity needed for the mixture viscosity. The other important settings of the phase coupling is summarized in Table 1.

Table 1. Mixture Model parameters and solver settings for CFD-DPM Coupling in Fluent.

Model Selections	
RANS Model	k-ϵ Realizable
Granular viscosity	Gidaspow
Granular bulk viscosity	Lun et al.
Frictional viscosity in particulate phase	neglected
Granular Temperature	Algebraic
Solid pressure	Lun et al.
Radial distribution	Lun et al.
Elasticity modulus	derived
Turbulent dispersion	DPM averaged
Restitution coefficient	0.97
Specularity coefficient	0.97
Solver settings	
Scheme	Phase Coupled SIMPLE
Gradient	Least Squared Cell Based
Pressure	PRESTO!
Momentum	Second Order Upwind
Volume fraction	Second Order Upwind
TKE	Second Order Upwind
Turbulent dissipation rate	Second Order Upwind
Transient formulation	Second Order Implicit

The mesh selection procedure was done by considering two factors: relative size of the pointwise particles to the cell size and the convergence of the gas phase flow. Herein, the difference between the Eulerian gas phase fields were indistinguishable between grid sizes of 1 mm and 5 mm cases (while using the k-ϵ turbulence model, as the wall function of the k-w model necessitates grids near wall much smaller than the minimum particle size) and we utilized a grid size of 5mm in all cases accordingly.

2.3. Case Study

The main focuses of the study are (i) to assess the how much the particle distribution is affected if we include the orientation information into the drag model statistically, (ii) analyse how informative the single particle force balance is to estimate the need for including the orientation information into a CFD study, (iii) and most importantly, what is the discrepancy between the commonly deployed spherical particle (Equation (8)) and non-spherical particle (Equation (9)) assumptions, and a non-spherical drag model that also takes the orientation information into account (Equation (2)). Accordingly, we selected a waste recovery unit as a case study in which non-spherical wood particles are separated from waste material under dilute flow conditions. The 2D chamber has a height of 3 m, with a diameter of 50 cm. Air is fed from the bottom through a diverging windbox (inlet = 40 cm, windbox outlet = 50 cm, height = 30 cm). The superficial gas velocity is set as either $5\,\mathrm{m\,s}^{-1}$ or $7.5\,\mathrm{m\,s}^{-1}$, for which the corresponding force balance acting on non-spherical wood particles are around the order of one. During the simulations, two different classes of

particles are fed: non-spherical wood particles and spherical waste material. Solid particles are injected 40 cm above the inlet with a velocity of $0.01\,\mathrm{m\,s^{-1}}$. Both particle classes exhibit Rosin-Rammler size distributions (Table 2). Particles that are entrained are collected from the top, while the rest is collected from the bottom. The width/height ratio, disengagement height, as well as the relative size of the wind box section are selected based on industrial particle separators.

Table 2. Phase properties deployed in the EL simulations for each phase.

Phase 1 (air)	
Density	$1.225\,\mathrm{kg\,m^{-3}}$
Viscosity	$1.789 \times 10^{-5}\,\mathrm{kg\,m^{-1}\,s^{-1}}$
Phase 2 (secondary, sand)	
Density	$2500\,\mathrm{kg\,m^{-3}}$
Particle shape	spherical
Minimum diameter	0.001 m
Mean diameter	0.003 m
Maximum diameter	0.01 m
Mass flow rate	$0.0075\,\mathrm{kg\,s^{-1}}$
Spread parameter	9.6
Number of diameters	30
Phase 3 (secondary, wood)	
Density	$400\,\mathrm{kg\,m^{-3}}$
Particle shape	cylindrical
Minimum equivalent diameter	0.001 m
Mean equivalent diameter	0.01 m
Maximum equivalent diameter	0.02 m
Mass flow rate	$0.0075\,\mathrm{kg\,s^{-1}}$
Spread parameter	9.6
Number of diameters	30

All simulations (2D) are done with ANSYS Fluent, where the gas phase is treated as a Eulerian continuum and the solid phase is represented by discrete Lagrangian parcels (see Section 2.2 for more details). The effect of secondary motion is investigated via deploying three drag models: (i) a custom probabilistic model integrated as a user defined function based on Hölzer-Sommerfeld correlation [26] (see Equation (2)), (ii) the native non-spherical model in Fluent (Haider and Levenspiel [20] (Equation (9)) that takes only particle shape into account through sphericity and (iii) base drag model for spherical particles (Equation (8)), which ignores both shape and orientation information (i.e., only uses d_{eq} information). The most formidable task here is the identification of the "orientation tendency" for a given mixture of particle classes. In the current study, experimental measurements of Cai et al. [25] was used to construct the probability density functions (PDFs) representing the orientation of cylindrical wood particles. In the Fluent User Defined Function implementation, the particle orientation (i.e., nutation angle) is randomly sampled from the experimental PDF for each bundle, at each iteration. Sampled particle orientations with respect to flow direction are then used to evaluate the drag coefficient of the Lagrangian particle parcel via the empirical model of Hölzer and Sommerfeld [26]. As a result, particle orientation tendencies are captured statistically throughout the chamber without noticeable computational effort.

It should be noted at this point that a thorough quantitative analysis of such a system would require detailed 3D simulations. In the current work, we conducted 2D simulations due to several reasons. Firstly, the study reports a qualitative comparison between different drag model approximations for "point-wise" Lagrangian particles, in an attempt to raise attention to the need for modelling the particle orientation-drag force relation in gas-solid flows. In particular, we compared the spherical particle and the native non-spherical particle assumptions with the Hölzer and Sommerfeld correlation, which considers both the orientation and the shape. Herein, the orientation of the actual particle is not resolved,

but statistically sampled from a distribution reported in the literature [25] and used to estimate the instantaneous drag coefficient of the particle bundles. Secondly, the studied problem has a very low volume fraction of particles, hence we do not expect much feedback from the particulate phase to the gas phase. Thirdly, the experimental study from which the orientation statistics are taken reports only averaged orientation distributions at 6 different heights and 5 different radial positions, implicitly assuming lateral symmetry. Furthermore, the experimental work showed that the orientation distribution was quite similar along the riser above 50 cm until the exit of the 3 m height test rig. The time-averaged radial orientation statistics were also similar in the riser in the annular region up to 0.9R (they observed a different distribution function near the wall as expected), particularly if we compare the variations with at different particle slenderness ratios [25]. It should be further noted that the orientation statistics were averaged over time scales much larger than the characteristic time scales of secondary motions of particles. With these considerations, we moot that such a statistical sampling would be sufficient enough to capture the qualitative distribution of particle bundles within the chamber and can provide evidence for the contrast between different drag models.

3. Results

3.1. Effect of Secondary Motion on Single Particles

The effects of secondary motion on the particle segregation tendencies were first tested on single particles by applying a force balance including (i) drag, (ii) gravitational and (iii) buoyancy forces. Following the case study, the non-spherical base particle shape is fixed as cylinder, while the effective shape is varied by changing the aspect ratio (AR). The particle properties (density, size, AR) are varied, and the corresponding force balance is calculated for a variety of nutation angles. This is done to answer the following questions:

- Given PSD, shape and flow conditions; how likely is it to experience the impact of secondary motion?
- Can we use force balance as an indicator for dilute flow conditions?

Figure 1 illustrates the variations in the calculated drag coefficients with the the drag model of Hölzer and Sommerfeld [26]. It is seen that as the particle shape diverges from the sphere (AR < 1 or AR > 1), the orientation information becomes critical and leads to logarithmic scale variations in the drag coefficients in the pneumatic conveying range (Figure 1a). It is worth noting here that the particle shape at velocities of interest also has a similar effect, creating log scale variations in the drag coefficient for the same equivalent diameter (Figure 1b). In other words, the effect of orientation is as significant as the shape information for Re > 1000, which is typically the case in the application.

In an attempt to test whether the orientation information can be simplified, we computed the error between the coefficient predicted by the Hölzer and Sommerfeld [26] and a simpler representation used in [14]:

$$C_{D,\phi} = C_{D,\phi=0^\circ} + (C_{D,\phi=90^\circ} - C_{D,\phi=0^\circ})sin^2\phi \tag{15}$$

Variations in relative percentage errors are shown in Figure 2. Comparisons indicate that even if the particle size and shape is fixed, averaging the drag coefficients over the orientation fails capturing the influence of particle orientation, particularly for Re > 1000, hence there is a need for a better representation of drag coefficients to reflect the secondary motion tendencies expected at high Re numbers.
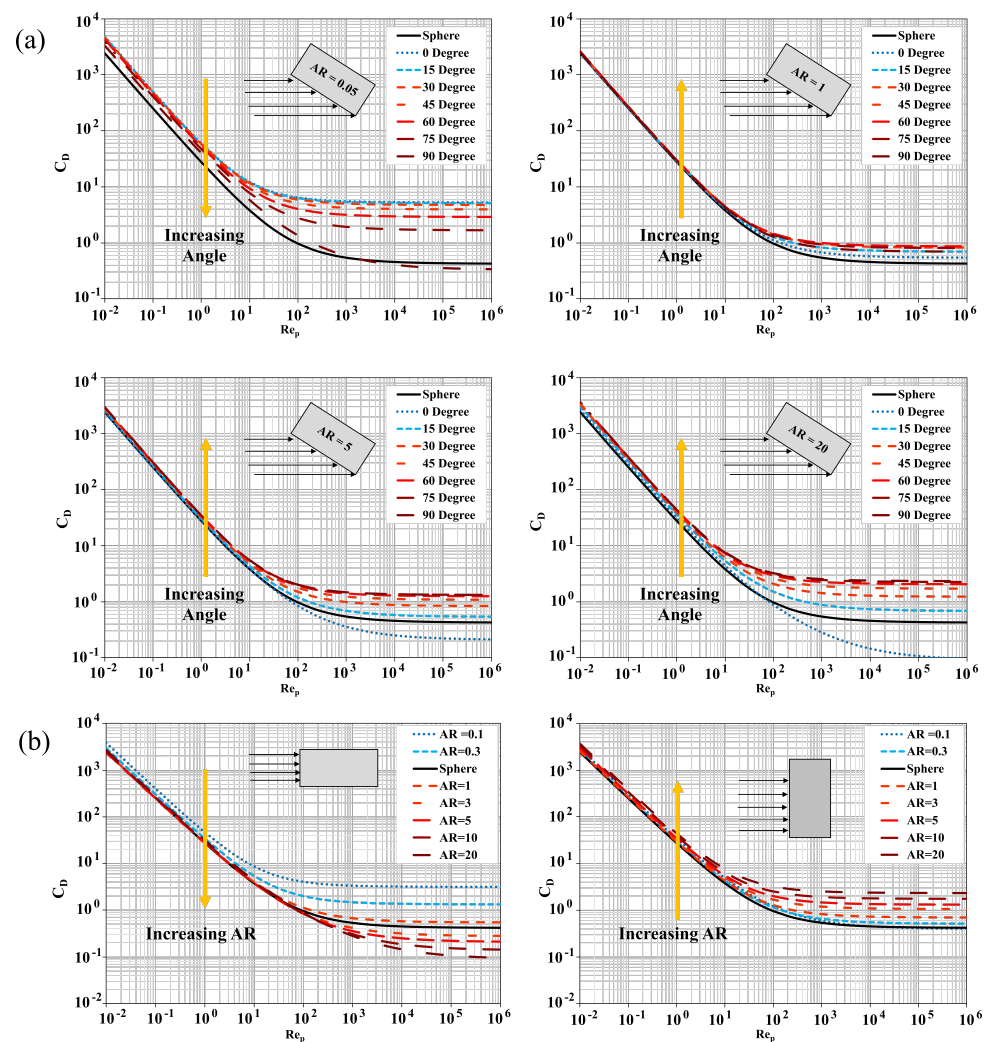
Figure 1. Comparison of drag coefficients (C_D) for a cylinder with an equivalent diameter of 3 mm. Each curve represents a different nutation angle at different aspect ratios. Spherical particle case (black curve) is added for comparison. (**a**) Each sub-figure reports the change in drag coefficient with increasing nutation angle at different aspect ratios. (**b**) Each sub-figure reports the change in drag coefficient with increasing aspect ratio at different two limiting orientations with respect to main flow direction. Note that for the studied particle cloud (Table 2), maximum expected Re for particles is 32,069.
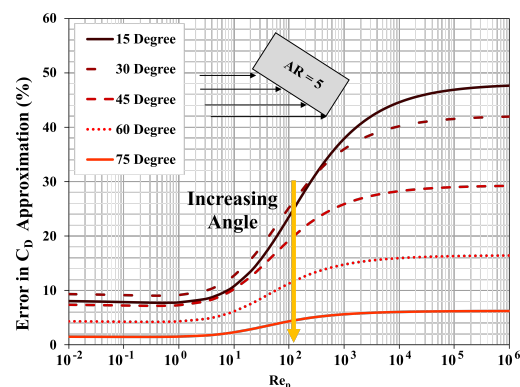
Figure 2. Relative percentage error between the Hölzer-Sommerfeld model (Equation (2)) and when weight-averaged orientation information (Equation (15)) is used for C_D at different nutation angles. Particle shape is cylindrical, with an equivalent diameter of 3 mm. Each curve represents a different nutation angle at different aspect ratios.

In an attempt to see how the secondary motion tendencies, hence the particle orientation with respect to flow, would manifest themselves in the force balance acting on particles (under dilute flow conditions), the ratio of drag forces to gravitational forces is displayed for possible orientation, shape and size combinations of a real particle mixture on parallel coordinates. Herein, vertical columns show the ranges of particle and flow related features such as (i) density, (ii) cylinder aspect ratio, (iii) equivalent diameter, (iv) nutation angle, (v) velocity, (vi) Re number and (vii) the computed drag coefficient with the Hölzer-Sommerfeld model. The column on the right yields the calculated force ratio (drag/modified gravity) in log-scale for a given feature combination. The results can be downloaded and further analyzed through the html file presented in the supporting material. Figure 3 shows the spread in the calculated force ratio for a given particle size distribution, nutation angle and the gas velocity (i.e., pink vertical lines. The html file can be used to pick different ranges to see the effect of each parameter). It is seen that when the particles exhibit secondary motions as reported in [25], the force ratio can change drastically. The effect of density shifts the force ratio distribution, but the spread in the force ratio is typically seen for the operating range of interest. For elongated particles, as in the case of wood recovery problem, if the particles have a wide range of size, shape and density distribution, there is a significant overlap with respect to the force ratios. This indicates that it becomes almost impossible to separate all with a fixed superficial gas velocity. Even if the particle mixture is prepared for a certain PSD and similar shapes, we see that the force balance ratio still fluctuates in log scale between positive and negative values, indicating that secondary motion will trigger complex particle mixing and segregation patterns. In other words, given a particle size, shape and density, there is not one, but many minimum fluidization velocities, for which the spread and the statistics are determined by the statistics of the particle orientation and shape. Similar variances have been also reported in the experimental measurement of drag coefficient of non-spherical particles [27]. This heuristic analysis reveals that the secondary motion will be influential for the case problem, which will be looked in detail via CFD simulations in the following sub-chapter systematically to quantify its impact and test whether such simple analysis can help us to determine the risks associated with secondary motion of particles.
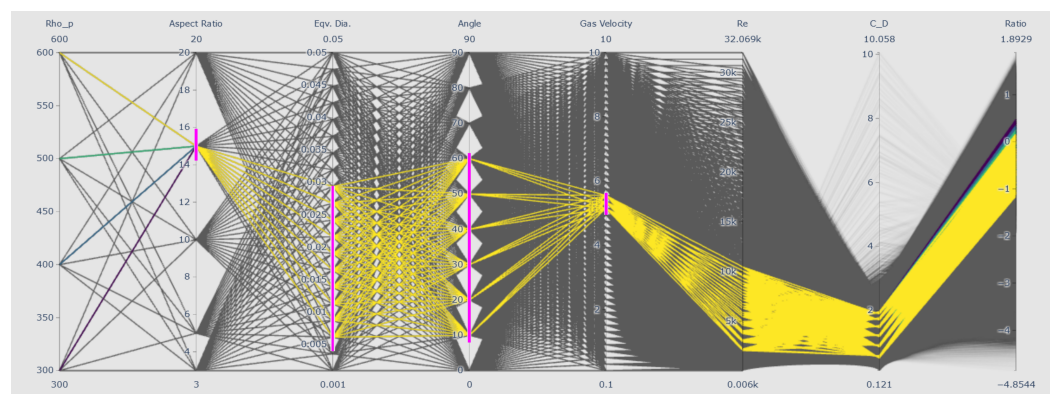

Figure 3. Possibility map for the force balance acting on particles for a variety of particle-flow interaction scenarios on parallel coordinates. Conditions relevant to the reference experiment and the CFD simulations are highlighted in color. The source html file can be found in the supplementary material.

3.2. Effect of Orientation on Particle Distribution at Low Velocities

In the previous section, it has been shown that particle orientation has a significant impact on the force balance acting on the individual particles. In this section, we will investigate parametrically (i) how the spread in the force balance can influence the particle segregation and distribution and (ii) how accurate the predictions obtained via spherical particle assumption and the shape corrector models available in Fluent. Herein, we will use the proposed probabilistic approach based on the Hölzer-Sommerfeld correlation as the benchmark solution. Details of the case study is described in Section 2.3.

In the first analysis, the superficial gas velocity is selected as $5\,\mathrm{m\,s^{-1}}$, where majority of the particles were expected not to be fluidized. This is based on the minimum fluidization velocity predicted by the Hölzer-Sommerfeld correlation at the most probable orientation ($\phi = 20°$). The resulting force balance predictions are illustrated in Figure 4. As can be seen from the figure, the model with the shape correction (Wood-Non-spherical) tends to overestimate the drag force acting on particles, compared the most probable orientation of particles. In practice, this would lead to underestimation of the segregation velocity, as it implies that wood can be separated from sand like particles (in average) at 5 m/s (R > 1). Nonetheless, with an averaged orientation data (most probable orientation with Hölzer-Sommerfeld model), it is seen that would not be the case. Furthermore, it is also revealed that spherical particle assumption drastically underestimates the drag forces, such that we cannot even identify a regime where they are separable, although it is quite possible when we take into account the orientation.
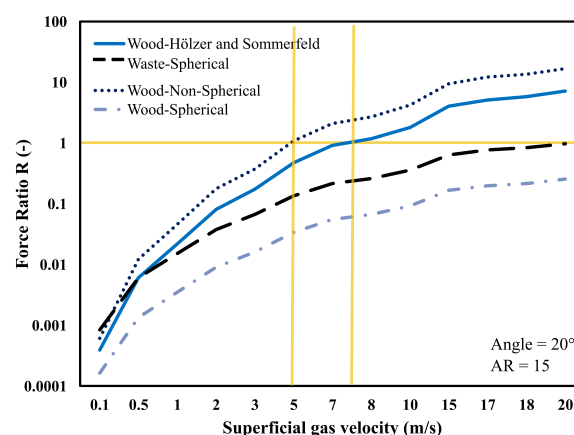
Figure 4. Force balance predictions estimated for averaged particle diameter and most probable orientation of the particles (Wood-Hölzer). The force ratio predicted by using the spherical (Wood-Spherical) and the non-spherical drag model with only consider the shape information (Wood-Non-spherical) are also shown for comparison, together with the spherical waste material relevant to the application.

The wood volume fractions at steady state conditions are depicted in Figure 5a at steady state conditions (t = 3 s). When the PSD and the orientation PDF are considered with the custom model, we still see that majority of the particles are not entrained but leave the chamber from the bottom boundary. Nonetheless, the distribution of the particles is affected by the fluctuations in the orientation with the PDF. That is not the case for the spherical particles, where they mainly fall downstream with their inertia, until they are forcibly bubbled at the gas inlet. On the other hand, when we only consider the shape correction in the drag model, the predictions tend to fail drastically and we see a large particle entrainment along the column, which does not reflect the reality.

The local distribution of particles becomes more visible when the particle trajectories are visualized with respect to their diameter (Figure 5b). Herein, a large portion of the PSD is being entrained with the shape corrector model, leading to quite a symmetric particle distribution. In the case of spherical assumption, only the very fine fractions are being carried with the flow. In the custom model, however, the distribution has local variations even at these low gas velocities. Yet, the longtime interval trajectories still reflect a symmetry. It is also seen that particles can be statistically entrained and get segregated (highlighted with yellow boxes), where the entrainment occurred stochastically. These comparisons indicate that particle orientation is very critical even for the conditions where particle entrainment is expected to be minimum.
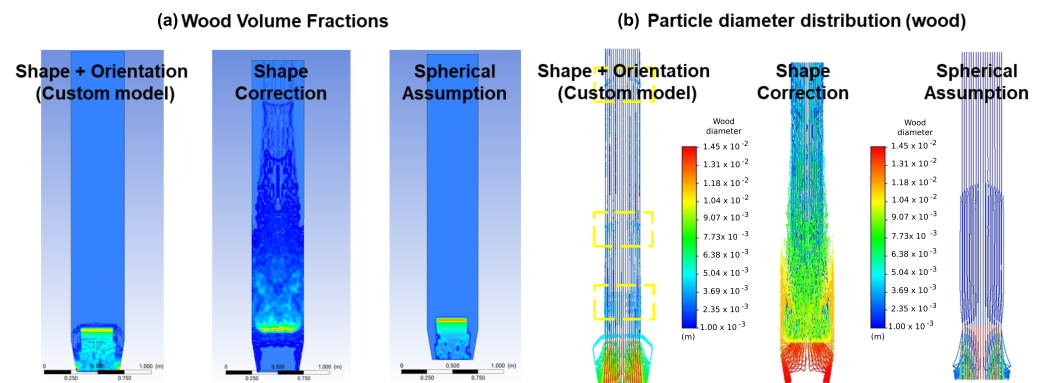
Figure 5. (**a**) Wood volume fraction predictions with three different drag models at steady conditions (t = 3 s). (**b**) Wood particle trajectories generated with three different drag models at steady conditions (t = 3 s). Color map indicates the particle diameter range.

3.3. Effect of Orientation on Particle Distribution Near Entrainment Velocities

In the next case, the superficial gas velocity is increased to $7.5\,\mathrm{m\,s^{-1}}$ to achieve entrainment for the mean particle size and the most probable condition. The corresponding force balance calculations are also given in Figure 4. From the force ratio (R), it is expected that there is a limited entrainment when we consider the secondary motion of particles, as R is expected to be around one (for the expected orientation). The statistical nature of the orientation, however, should disperse the entrainment. Figure 6a shows the wood volume fractions and particle trajectories for the custom model based on the Hölzer-Sommerfeld correlation and the spherical particle assumption. As expected, the secondary motion represented by stochastically sampled orientations (based on the reference experiment) leads to complex particle mixing patterns and segregation even around the minimum fluidization flow conditions. The flow patterns were found to be highly nonlinear for the particles. Nonetheless, spherical assumption leads to underestimation of both entrainment and the particle mixing patterns.
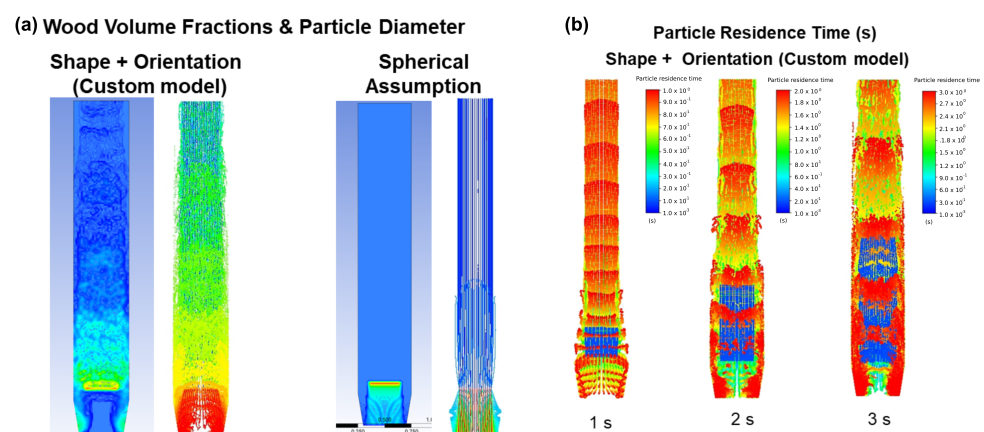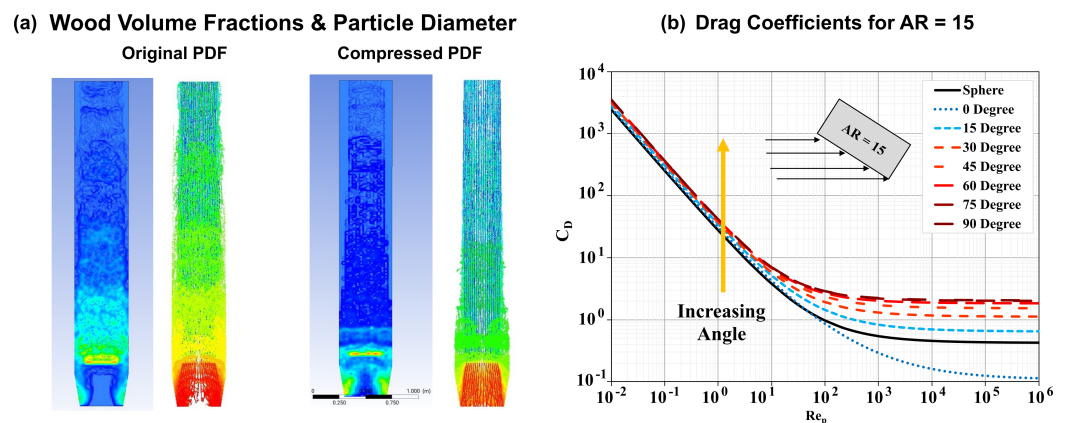

Figure 6. (**a**) Wood volume fractions and the particle trajectories generated with two different drag models at steady conditions (t = 3 s). Color map indicates the volume fractions and the particle diameter range, respectively. (**b**) Particle residence time distributions for wood parcels at three different physical times. Color map indicates the time range for each frame.

The particle mixing and segregation patterns get more visible if the residence time distribution of the Lagrangian phase is investigated. Figure 6b shows the residence times of particle bundles at three different times. Segregation emerges even at early process times, in which the entrained particles typically not mixed but carried with the flow in a non-continuous manner. The particle residence times for a given fraction is also spread even for the same diameter particles, indicating the impact of the orientation of

the particle distribution. In other words, due to fluctuations in the drag force with the orientation, average residence time of the particles do increase, which in turn effectively increases the particle disengagement height. This is of particular importance especially for reactive systems.

3.4. Effect of Secondary Motion Tendencies on Particle Segregation

In order to test the impact of the orientation tendency further, the numerical analysis is extended with an artificial orientation probability distribution, where the spread of the original distribution is halved [25]. Figure 7a illustrates the wood volume fractions and the particle diameter distributions for both the original orientation PDF and the artificially compressed statistics. The effect of the spread of orientation tendency is immediately visible on both wood volume fractions and the particle trajectories of mid-size (green) particle trajectories. In a limited chamber height, when the particle orientation statistics become wide, particles have a much higher chance to be entrained and leave the system from the top, compared to smaller fluctuations in the probability distribution function. In other words, as the particles tend to rotate more frequently, the impact of orientation information gets more significant at finite chamber heights. This is a direct result of the increased transport disengagement height.

Figure 7. (**a**) Wood volume fractions and the particle trajectories generated with two different orientation PDFs at steady conditions (t = 3 s). Color map indicates the volume fractions and the particle diameter range respectively. (**b**) Fluctuations in particle drag coefficients for cylinders of AR = 15 with changing nutation angles. Note that particle of interests has high particle Re numbers.

The underlying reason can be traced in the force balance acting on particles. Figure 7b shows the changing drag coefficient for a cylindrical particle with changing orientations for the same aspect ratio. When the orientation statistics do jump more frequently between 10° and 60° as in the experimental data [25], the corresponding drag coefficient do change in the log scale and gets separated from simple, sphere like behaviour. As the nutation angle variations decrease, the jump in the drag coefficient variations are reduced. This change is then reflected on the drag force, which in turn changes the particle mixing and entrainment patterns.

3.5. Effect of Particle Shape on Particle Segregation

Particle shape is another important factor determining the relative significance of orientation information on the drag coefficients (see Figure 1). In an attempt to test its effect on the particle distribution and segregation, the same orientation tendency data (i.e., PDF function) is used parametrically. Particle volume fraction distributions of three cases are shown in Figure 8. The results show that as the particle shape gets closer to the spherical particles, the influence of orientation gets smaller, but still has a profound effect on the particle distributions. For AR = 3, particle tends to be less entrained as expected, but the

expansion of the particle bed is very different compared to the spherical case. Furthermore, there is still a significant entrainment given the limited chamber height.

Wood Volume Fractions
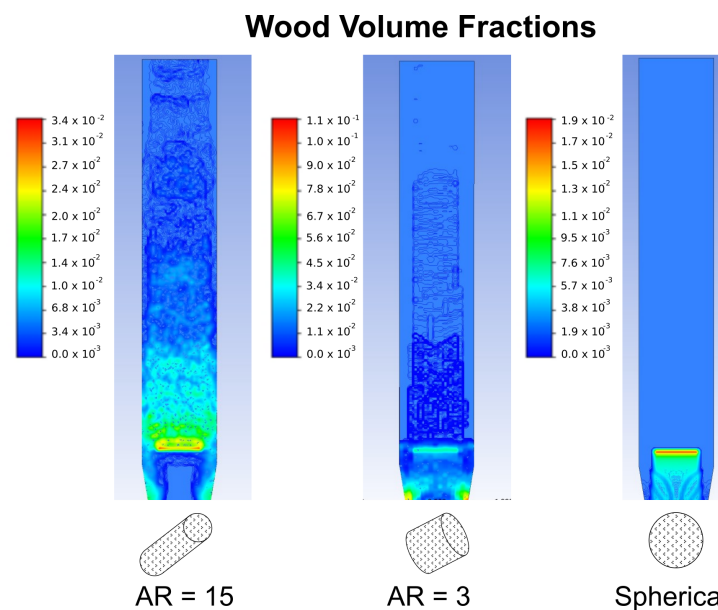
Figure 8. Wood volume fraction predictions with three different particle shapes at steady conditions (t = 3 s). Cylindrical particle flows are modeled with the custom drag model.

The effect of shape can again be traced when the force balance for the averaged particle properties is investigated. Figure 1b depicts the variations in drag coefficients with changing shape, i.e., aspect ratios of cylinders. One interesting observation here is the change in trends with respect to the nutation angles. When particles are aligned with respect to flow, elongated particles yield much lower drag coefficients compared to cylindrical particles. On the contrary, the trend is just the opposite when particles are perpendicular to the flow direction. In both cases, however, particle behaviour diverges in log scale as the shape gets diverged from spherical symmetry. These results highlight that in real applications where the particles are rarely spherical, the effect of shape and orientation leads to very complex behaviour, which changes the particle distribution within the chamber. More importantly, such physics can not be captured if the drag force models do not include that information.

3.6. Effect of Secondary Motion on Flow at Macro Scale

It is seen that particle orientation has a significant impact on the local particle mixing patterns in the chambers, which is of significant importance particularly for reactive systems. For particle separators, however, local fluctuations may diminish and lose their importance if the chamber height (or residence time) is long enough to smoothen these variations. In order to see the effect of secondary motion on the flow at macro-scale, we examined the amount of wood particles collected at the chamber exit in time.

Figure 9 shows the discrepancy between the predicted relative wood mass flow rates at the top exit boundary for all cases presented so far (steady state conditions, t = 3 s). It is seen that when the particle orientation information is ignored, the model predictions even for global quantities do change drastically. It is seen that (i) shape correction leads to over-estimation even at low velocities, (ii) spherical assumption also fails disrespectful of the operating range, (iii) orientation tendency is critical in all cases and (iv) difference gets more critical as the particle shape diverges from spherical behaviour. The results highlight that orientation information is very critical to capture the particle phase flow and has a strong impact even at global quantities.
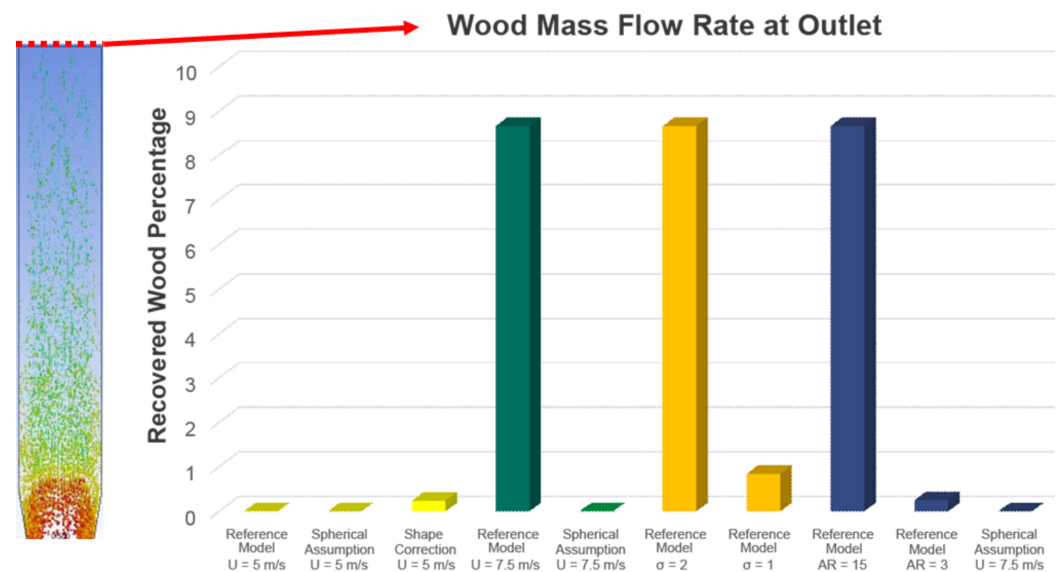
Figure 9. Recovered wood percentage at the chamber outlet. The percentage values are calculated with respect to the wood inlet at steady conditions (t = 3 s).

These parametric comparisons highlight that particle orientation statistics are extremely important to capture the particle mixing and segregation patterns at dilute regime, which gets even more important if the system includes multi-physics phenomena (e.g., reactive systems [45], heat transfer problems [46]), as it non-linearly determines how the particle distributions change dynamically within a chamber, which in turn dictates the spatial and temporal distribution of the effective interfacial area in a transport problem. Hence, there is a need for further research to expand the know-how on these complex flows to be able to design and optimize gas-solid flow chambers accurately.

4. Conclusions

Many industrial processes, such as gasification, coating and conveying, involve complex interactions between the particulate and the gas phase. Accordingly, accurate description of the turbulent gas–solid flow becomes a critical for industrial design and optimization problems. Variations in the particle properties, however, complicate the flow analysis for such systems, especially for the description of the fluid-particle interactions. In most cases, particles are treated as spherical, pointwise objects for the sake of simplicity, despite the experimental evidence showing the strong relationship between drag forces, particle orientation and shape. In this work, the effect of secondary motion of particles in multi-phase gas-solid flows was investigated parametrically for a pneumatic conveying problem at dilute flow regime. Predictive accuracy of the simplifying model assumptions on drag coefficient models were tested on three aspects of the problem: superficial gas velocity, secondary motion tendencies and particle shape at micro and macro mixing levels.

Sensitivity analysis on the drag coefficient revealed that the drag coefficient can vary in log-scale when either the particle orientation or the shape of the function changes. More importantly, even for a given particle shape and a fixed equivalent diameter, the ratio between the drag and gravitational forces can exhibit these large variations with changing particle orientation. Therefore, even fundamental properties such as minimum fluidization velocity is affected by the orient ion tendencies of the particles due to secondary motions. The results further showed that both spherical particle assumption and shape correction with sphericity leads to large errors in both particles drag properties and the resulting particle segregation and separation at high particle Re regime. Spherical particle assumption leads to under-estimation of the drag on elongated particles such as recycled wood, while the correcting only for the shape information leads to strong overestimation. The orientation tendency information was found to be critical for particle distribution even at low velocities,

where the particle entrainment is minimum. In such a case, particle fluidization and mixing patterns do change significantly when orientation information is included in the drag model. Furthermore, as the shape of the particle diverges from the spherical shape, the impact of secondary motion gets more critical. Even when the orientation statistics are artificially reduced by halving the spread of the probability density functions, the impact of the secondary motion was still visible. When the macroscopic quantities such as wood recovery percentages are compared, it was found that orientation has a strong impact even when macro-mixing patterns are smoothened at longer residence times.

Nomenclature

The following symbols are used in this manuscript:

Greek letters

α	volume fraction
ϵ	rate of dissipation of turbulent kinetic energy
θ	nutation angle
ϕ	sphericity
μ	Dynamic viscosity
ν	Kinematic viscosity
ρ	Density
τ_r	particle relaxation time

Latin letters

AR	Aspect ratio of cylindrical particles
C_d	Drag coefficient
d	diameter
F	forces affecting the particle trajectory
g	Gravitational acceleration
R	Force ratio
Re	Reynolds number
u	velocity

Subscripts and superscripts

dr	drift velocity
eq	equivalent
f	fluid
m	mixture
n	number of phases
p	particle

References

1. Ergun, S.; Orning, A.A. Fluid Flow through Randomly Packed Columns and Fluidized Beds. *Ind. Eng. Chem.* **1949**, *41*, 1179–1184. [CrossRef]
2. Wen, C.Y.; Yu, Y.H. A generalized method for predicting the minimum fluidization velocity. *AIChE J.* **1966**, *12*, 610–612.
3. Syamlal, M.; O'Brien, T.J. Computer simulation of bubbles in a fluidized bed. *AIChE Symp. Ser.* **1989**, *85*, 22–31.
4. Huilin, L.; Gidaspow, D. Hydrodynamics of binary fluidization in a riser: CFD simulation using two granular temperatures. *Chem. Eng. Sci.* **2003**, *58*, 3777–3792. [CrossRef]
5. Hill, R.J.; Koch, D.L.; Ladd, A.J.C. Moderate-Reynolds-number flows in ordered and random arrays of spheres. *J. Fluid Mech.* **2001**, *448*, 243–278. [CrossRef]
6. Beetstra, R.; van der Hoef, M.A.; Kuipers, J.A.M. Drag force of intermediate Reynolds number flow past mono- and bidisperse arrays of spheres. *AIChE J.* **2007**, *53*, 489–501.
7. Tenneti, S.; Garg, R.; Subramaniam, S. Drag law for monodisperse gas–solid systems using particle-resolved direct numerical simulation of flow past fixed assemblies of spheres. *Int. J. Multiph. Flow* **2011**, *37*, 1072–1092. [CrossRef]
8. Tang, Y.; Peters, E.A.J.F.; Kuipers, J.A.M. Direct numerical simulations of dynamic gas-solid suspensions. *AIChE J.* **2016**, *62*, 1958–1969.
9. Stanly, R.; Shoev, G. Detailed analysis of recent drag models using multiple cases of mono-disperse fluidized beds with Geldart-B and Geldart-D particles. *Chem. Eng. Sci.* **2018**, *188*, 132–149. [CrossRef]
10. Mandø, M.; Rosendahl, L. On the motion of non-spherical particles at high Reynolds number. *Powder Technol.* **2010**, *202*, 1–13. [CrossRef]
11. Castang, C.; Laín, S.; Sommerfeld, M. Pressure center determination for regularly shaped non-spherical particles at intermediate Reynolds number range. *Int. J. Multiph. Flow* **2021**, *137*, 103565. [CrossRef]
12. Richter, A.; Nikrityuk, P.A. New correlations for heat and fluid flow past ellipsoidal and cubic particles at different angles of attack. *Powder Technol.* **2013**, *249*, 463–474. [CrossRef]
13. Zastawny, M.; Mallouppas, G.; Zhao, F.; van Wachem, B. Derivation of drag and lift force and torque coefficients for non-spherical particles in flows. *Int. J. Multiph. Flow* **2012**, *39*, 227–239. [CrossRef]
14. Ouchene, R.; Khalij, M.; Arcen, B.; Tanière, A. A new set of correlations of drag, lift and torque coefficients for non-spherical particles and large Reynolds numbers. *Powder Technol.* **2016**, *303*, 33–43. [CrossRef]
15. Guan, Y.; Guadarrama-Lara, R.; Jia, X.; Zhang, K.; Wen, D. Lattice Boltzmann simulation of flow past a non-spherical particle. *Adv. Powder Technol.* **2017**, *28*, 1486–1494. [CrossRef]
16. Mahajan, V.V.; Nijssen, T.M.; Kuipers, J.A.; Padding, J.T. Non-spherical particles in a pseudo-2D fluidised bed: Modelling study. *Chem. Eng. Sci.* **2018**, *192*, 1105–1123. [CrossRef]
17. Chen, Y.; Jiang, P.; Xiong, T.; Wei, W.; Fang, Z.; Wang, B. Drag and heat transfer coefficients for axisymmetric nonspherical particles: A LBM study. *Chem. Eng. J.* **2021**, *424*, 130391. [CrossRef]
18. Buettner, K.E.; Curtis, J.S.; Sarkar, A. Fluid-particle drag force measurements from particle-resolved CFD simulations of flow past random arrays of ellipsoidal particles. *Chem. Eng. Sci.* **2021**, *235*, 116469. [CrossRef]
19. van Wachem, B.; Zastawny, M.; Zhao, F.; Mallouppas, G. Modelling of gas-solid turbulent channel flow with non-spherical particles with large Stokes numbers. *Int. J. Multiph. Flow* **2015**, *68*, 80–92. [CrossRef]
20. Haider, A.; Levenspiel, O. Drag coefficient and terminal velocity of spherical and nonspherical particles. *Powder Technol.* **1989**, *58*, 63–70. [CrossRef]
21. Ganser, G.H. A rational approach to drag prediction of spherical and nonspherical particles. *Powder Technol.* **1993**, *77*, 143–152. [CrossRef]
22. Tran-Cong, S.; Gay, M.; Michaelides, E.E. Drag coefficients of irregularly shaped particles. *Powder Technol.* **2004**, *139*, 21–32. [CrossRef]
23. Dioguardi, F.; Mele, D. A new shape dependent drag correlation formula for non-spherical rough particles. Experiments and results. *Powder Technol.* **2015**, *277*, 222–230. [CrossRef]
24. Bagheri, G.; Bonadonna, C. On the drag of freely falling non-spherical particles. *Powder Technol.* **2016**, *301*, 526–544. [CrossRef]
25. Cai, J.; Peng, Z.; Wu, C.; Zhao, X.; Yuan, Z.; Moghtaderi, B.; Doroodchi, E. Numerical Study of the Orientation of Cylindrical Particles in a Circulating Fluidized Bed. *Ind. Eng. Chem. Res.* **2016**, *55*, 12806–12817. [CrossRef]
26. Hölzer, A.; Sommerfeld, M. New simple correlation formula for the drag coefficient of non-spherical particles. *Powder Technol.* **2008**, *184*, 361–365. [CrossRef]
27. Krueger, B.; Wirtz, S.; Scherer, V. Measurement of drag coefficients of non-spherical particles with a camera-based method. *Powder Technol.* **2015**, *278*, 157–170. [CrossRef]
28. Sanjeevi, S.K.; Kuipers, J.A.; Padding, J.T. Drag, lift and torque correlations for non-spherical particles from Stokes limit to high Reynolds numbers. *Int. J. Multiph. Flow* **2018**, *106*, 325–337. [CrossRef]
29. Hilton, J.E.; Cleary, P.W. The influence of particle shape on flow modes in pneumatic conveying. *Chem. Eng. Sci.* **2011**, *66*, 231–240. [CrossRef]
30. Ma, H.; Zhao, Y. Investigating the fluidization of disk-like particles in a fluidized bed using CFD-DEM simulation. *Adv. Powder Technol.* **2018**, *29*, 2380–2393. [CrossRef]

31. Mema, I.; Wagner, E.C.; van Ommen, J.R.; Padding, J.T. Fluidization of spherical versus elongated particles—Experimental investigation using X-ray tomography. *Chem. Eng. J.* **2020**, *397*, 125203. [CrossRef]

32. Roostaee, A.; Vaezi, M. Developing a standard platform to predict the drag coefficient of irregular shape particles. *Powder Technol.* **2022**, *395*, 314–337. [CrossRef]

33. Zhou, H.; Flamant, G.; Gauthier, D.; Lu, J. Numerical simulation of the turbulent gas-particle flow in a fluidized bed by an LES-DPM model. *Chem. Eng. Res. Des.* **2004**, *82*, 918–926. [CrossRef]

34. Toschi, F.; Bodenschatz, E. Lagrangian Properties of Particles in Turbulence. *Annu. Rev. Fluid Mech.* **2009**, *41*, 375–404.

35. Balachandar, S.; Eaton, J.K. Turbulent Dispersed Multiphase Flow. *Annu. Rev. Fluid Mech.* **2010**, *42*, 111–133.

36. Mallouppas, G.; van Wachem, B. Large Eddy Simulations of turbulent particle-laden channel flow. *Int. J. Multiph. Flow* **2013**, *54*, 65–75. [CrossRef]

37. Yuan, W.; Andersson, H.I.; Zhao, L.; Challabotla, N.R.; Deng, J. Dynamics of disk-like particles in turbulent vertical channel flow. *Int. J. Multiph. Flow* **2017**, *96*, 86–100. [CrossRef]

38. Mathai, V.; Lohse, D.; Sun, C. Bubbly and Buoyant Particle–Laden Turbulent Flows. *Annu. Rev. Condens. Matter Phys.* **2020**, *11*, 529–559.

39. Zhong, W.; Yu, A.; Liu, X.; Tong, Z.; Zhang, H. DEM/CFD-DEM Modelling of Non-spherical Particulate Systems: Theoretical Developments and Applications. *Powder Technol.* **2016**, *302*, 108–152. [CrossRef]

40. Ke, C.; Shu, S.; Zhang, H.; Yuan, H.; Yang, D. On the drag coefficient and averaged Nusselt number of an ellipsoidal particle in a fluid. *Powder Technol.* **2018**, *325*, 134–144. [CrossRef]

41. Liu, R.J.; Xiao, R.; Ye, M.; Liu, Z. Analysis of particle rotation in fluidized bed by use of discrete particle model. *Adv. Powder Technol.* **2018**, *29*, 1655–1663. [CrossRef]

42. Kuang, S.; Zhou, M.; Yu, A. CFD-DEM modelling and simulation of pneumatic conveying: A review. *Powder Technol.* **2020**, *365*, 186–207.

43. Zhang, Y.; Xu, J.; Chang, Q.; Zhao, P.; Wang, J.; Ge, W. Numerical simulation of fluidization: Driven by challenges. *Powder Technol.* **2022**, *414*, 118092. [CrossRef]

44. Morsi, S.A.; Alexander, A.J. An investigation of particle trajectories in two-phase flow systems. *J. Fluid Mech.* **1972**, *55*, 193–208. [CrossRef]

45. Wang, J.; Yang, Z.; Wang, M. Effect of non-spherical particles on burning behavior during aluminum combustion. *Particuology* **2020**, *51*, 173–183. [CrossRef]

46. Ates, C.; Selçuk, N.; Kulah, G. Significance of particle concentration distribution on radiative heat transfer in circulating fluidized bed combustors. *Int. J. Heat Mass Transf.* **2018**, *117*, 58–70. [CrossRef]